Reconstructing the cosmic Horseshoe gravitational lens using the singular perturbative approach.

C. Alard

Reconstructing the cosmic horseshoe gravitational lens using the singular perturbative approach

C. Alard[★]

IAP, 98bis Boulevard Arago, F-75014 Paris, France

ABSTRACT

The reconstruction of the cosmic horseshoe gravitational lens using the perturbative method reveals the presence of significant third-order terms. The presence of these higher order terms is apparent in the numerical expansion of the perturbative fields in Fourier series. The expansion of the fields at order 2 produces a higher value of the chi-square. Expanding at order 3 provides a very significant improvement, while order 4 does not bring a significant improvement over order 3. The presence of the order 3 terms is not a consequence of limiting the perturbative expansion to the first order. The amplitude and signs of the third-order terms are recovered by including the contribution of the other group members. This analysis demonstrates that the fine details of the potential of the lens could be recovered independently of any initial assumptions by using the perturbative approach.

Key words: gravitational lensing: strong – methods: numerical.

1 INTRODUCTION

Strong gravitational lensing offers a unique opportunity to probe the dark haloes potential in the vicinity of the Einstein circle. The lensing potential relates directly to the projected matter distribution and as a consequence is a direct measurement of the matter distribution in the lens. However, deriving a precise relation between the observations of a gravitational lens and the lensing potential is generally difficult. There are basically two main problems. First, the lens may show some degree of complexity and may not be properly described with simple analytical models. And secondly, some degree of degeneracy in the modelling of the lens is generally present, see for instance, Saha & Williams (2006), Wucknitz (2002) and Chiba & Takahashi (2002). A solution to the first point is to use a general, model-free method for the reconstruction of the potential. A simple example of a general method is to use a grid to reconstruct the potential. However, the obvious drawback is that the grid introduces many free parameters and thus aggravates the degeneracy issue. The example of the grid illustrates the intrinsic difficulty to develop a method that is both model independent and not prone to degeneracy issues. A number of solutions to these issues have been studied in the literature. The first group of solutions is based on the introduction of constraints on the model. It is obvious that introducing proper constraints in the model reduces degeneracy and also the likelihood of false solutions. An example of such constraints is given by the introduction of regularization schemes for the source, see for instance, Warren & Dye (2003) and Suyu et al. (2006). Another solution is to use a specialized potential expansion like Evans & Witt (2003) or Trotter, Winn & Hewiit (2000). The merit of these

expansions is to explore models with large degrees of freedom but relatively low levels of degeneracy. And finally, another option is to assume some initial guess for the potential and to refine this guess using a general numerical scheme. Example of this approach can be found in Vegetti & Koopmans (2009) and Suyu et al. (2009). Provided that the initial assumption about the potential model is justified, these methods offer an interesting exploration of the parameter space in the vicinity of the initial guess. An interesting way to tackle the degeneracy problem is to develop a method that offers a direct relation between the arc morphology and the potential. This is precisely what the perturbative approach (Alard 2007) achieves. Some specific examples of reconstruction of arc systems using the perturbative approach are presented in Alard (2009) and Alard (2010). In particular, the reconstruction of the lens in Alard (2009) shows that very complex systems can be handled in this approach. The application of the perturbative method to the cosmic horseshoe gravitational lens offers the possibility to push the reconstruction to a high level of accuracy. The *Hubble Space Telescope* (*HST*) data available for this lens offer an excellent resolution and a wealth of details allowing us to probe the fine details of the halo dark matter distribution. However, it is important to note that no additional data like for instance kinematic data are available for the cosmic horseshoe lens. As a consequence, it will not be possible to perform the interesting cross-analysis performed in Czoske et al. (2008), Barnabè et al. (2009), Barnabè et al. (2011) and Czoske et al. (2012).

1.1 The perturbative approach

This section will recall the basics of the first-order perturbative method presented in Alard (2007). In strong gravitational lensing,

★ E-mail: alard@iap.fr

the response to a small perturbation can be large. This high degree of non-linearity does not seem compatible with a perturbative expansion, especially a first-order expansion. However, it is important to note that for tangential gravitational arcs the non-linearity is in the angular coordinate. The amplitude of the response to a perturbation in the radial coordinate is much smaller. This suggests that the perturbative expansion should be performed using the radial coordinate. But it does not solve the problem of the high non-linearity in the angular domain. This issue is solved by introducing a special perturbative framework. To develop this framework, let us consider a point source situated at the centre of a circularly symmetric lens. Due to the symmetry of the potential, the image of the central point source is an infinity of points situated on a circle. The radius of this perfect ring is the Einstein radius. For convenience, the Einstein radius is normalized to unity by using a proper choice of units. The infinite number of images on the circle is located at all angular positions. As a consequence at any angular position, an image of the central point exists. Let us define this perfect ring situation as the unperturbed situation. Thus, for any image formed in a perturbed situation at angular position θ an image on the unperturbed unit circle will also exist at the same angular position θ. As a consequence, the perturbed image can be considered as a perturbation only in the radial direction of the specific unperturbed image at the same angular position. Thus, the response to a general perturbation $\psi(r, \theta)$ of the circular potential $\phi_0(r)$ is a radial displacement dr of the image. The displacement dr is of the same order as the potential perturbation. The general expression for the potential reads

$$\phi(r, \theta) = \phi_0(r) + \epsilon \psi(r, \theta). \tag{1}$$

And the radial response is

$$r = 1 + \epsilon dr, \tag{2}$$

where $\epsilon \ll 1$. Let us now consider a perturbed situation where the source is not exactly at the centre of the circular potential but has a small impact parameter R_S of the order of ϵ. Thus,

$$R_S = \epsilon r_S. \tag{3}$$

We are now ready to introduce the perturbative expansions of equations (1)–(3) in the lens equation. The lens equation reads

$$\boldsymbol{R}_S = \boldsymbol{r} - \nabla\phi. \tag{4}$$

Developing the lens equation to the first order in ϵ leads to

$$\boldsymbol{r}_S = (\kappa_2 \, dr - f_1) \boldsymbol{u}_r - \frac{df_0}{d\theta} \boldsymbol{u}_\theta \tag{5}$$

with

$$f_1 = \left[\frac{d\psi}{dr} \right]_{r=1}; \qquad f_0 = \psi(1, \theta); \qquad \kappa_2 = 1 - \frac{d^2\phi_0}{dr^2}. \tag{6}$$

It is useful to introduce the impact parameter of the source, namely $\boldsymbol{r}_S = \tilde{r}_S + r_0$ leading to

$$\tilde{\boldsymbol{r}}_S = \left(\kappa_2 \, dr - \tilde{f}_1 \right) \boldsymbol{u}_r - \frac{d\tilde{f}_0}{d\theta} \boldsymbol{u}_\theta \tag{7}$$

with

$$\tilde{f}_i = f_i + x_0 \cos(\theta) + y_0 \sin(\theta), \quad i = 0, 1.$$

And the impact parameter vector $\boldsymbol{r}_0$

$$\boldsymbol{r}_0 = (x_0, y_0).$$

The fields f_1 and $\frac{df_0}{d\theta}$ have direct and simple physical meaning. To illustrate this direct relation to the observation we will now consider a circular source. It is straightforward to solve equation (7) and obtain the images of the circular contour of the source. For a contour with radius r_0, equation (7) is of second order in dr leading to the following two solutions,

$$\kappa_2 dr = \tilde{f}_1 \pm \sqrt{r_0^2 - \frac{d\tilde{f}_0}{d\theta}^2}. \tag{8}$$

Equation (8) provides a direct relation between the contours of the images and the perturbative fields $\tilde{f}_1$ and $\frac{d\tilde{f}_0}{d\theta}$. The field $\tilde{f}_1$ is the mean position of the image contour at each angular position θ. While the field $\frac{d\tilde{f}_0}{d\theta}$ is related to the angular extent of the images. The field $\frac{d\tilde{f}_0}{d\theta}$ is zero at the centre of the image and has precisely the value r_0 at the image edge. As a consequence, the morphology of the fields $\frac{d\tilde{f}_0}{d\theta}$ controls the formation of the images. This direct relation between the theory and the observations is a unique feature of the perturbative model. It is interesting to emphasize at this point that other methods that could appear similar to the perturbative approach are not equivalent. For instance, the model developed in Evans & Witt (2003) is not as general as the perturbative expansion. This model would be equivalent to a single field perturbative expansion, or to say it differently that the second field would be a fixed dependence of the first one. In the same spirit, it is also interesting to note that the Trotter et al. (2000) Fourier expansion is not equivalent to a Fourier series expansion of the perturbative fields. The actual Trotter et al. (2000) expansion requires more coefficients than the corresponding Fourier series expansion of the fields. It is also clear that by no mean it is required to expand the perturbative fields in Fourier series, any other representation of the fields is possible. The main interest of the Fourier series expansion of the fields is the direct relation with the multipole expansion at the Einstein radius. Since this relation also allows the formal separation of contributions inside and outside the Einstein radius. In order to exploit the relation to the multipole expansion, the Fourier series expansion of the fields will be adopted in this paper. To conclude this introduction on the perturbative method, it is important to note that a single perturbative expansion does not relate to a single model but rather to a general class of models. Furthermore, such a class contains an infinite number of models. This is a clear illustration of the general degeneracy present in modelling gravitational lenses.

2 BUILDING THE PERTURBATIVE SOLUTION

In the perturbative approach (Alard 2007, 2009, 2010), the construction of the solution requires the evaluation of the two fields f_1 and $\frac{df_0}{d\theta}$. These two quantities are functional of the angular variable in the lens plane θ.

2.1 Initial approximation

The circular source model is used as a first guess in order to estimate the parameters of a piecewise polynomial model of the fields. The reconstruction of f_1 is direct, while $\frac{df_0}{d\theta}$ is estimated using the following constraints, the field is near zero in the central region of each images, and the field is above a threshold value in the dark areas. In this particular lens, the nature of the first guess is simplified since the structure of the images reveals a fold configuration. The initial estimation of f_1 is done by taking the mean position of the bright spots in the image. An estimation of f_1 can also be done by estimating the closest fold configuration. These two estimates give quite similar results and are both appropriate as a first guess. A similar

approach is used for $\frac{df_0}{d\theta}$, one can reconstruct the field by estimating its local behaviour near the nodes and make an interpolation with the constraint that the field must be above a certain threshold in the dark areas. Taking the closest fold configuration gives also similar results for $\frac{df_0}{d\theta}$. This initial guess is consistent with the topological properties of the solution and is an approximate description of its general shape. To reach the optimal level of accuracy, this solution needs to be refined numerically. The numerical refinement could be performed directly on the polynomial piecewise elements, but since the Fourier expansion of the fields is related to the multipole expansion of the potential, it is more efficient to expand the fields using Fourier series,

$$\begin{cases} f_1 = \sum_n \alpha_{1,n} \cos(n\theta) + \beta_{1,n} \sin(n\theta) \\ \frac{df_0}{d\theta} = \sum_n \alpha_{0,n} \cos(n\theta) + \beta_{0,n} \sin(n\theta) \end{cases}. \quad (9)$$

2.2 Source and image reconstruction

The first step in the construction of the refined numerical model is to make an initial estimation of the Fourier series coefficients. This is easily accomplished by computing the scalar product of the Fourier basis functions with the piecewise polynomial model. Once the Fourier coefficients are initiated, the optimal value of the coefficients are computed by minimizing the chi-square between the re-constructed image of the source and the *HST* data. The reconstruction of the source and its associated images are complex processes. Many interesting papers describe this process in detail, for instance, Tagore & Jackson (2016), Jackson et al. (2015), Birrer, Amara & Refregier (2015), Birrer et al. (2014), Brownstein et al. (2012) and Bolton et al. (2012). We will now describe in details the source reconstruction method used in this work. The accurate reconstruction of the source and of its associated images requires to work at a resolution in the image plane smaller than the pixel size. As a consequence, a finer grid in the image plane is formed by subdividing the pixels. The typical over-resolution is of a factor of 10 in each direction. The values of the image on the subgrid are obtained by B-spline interpolation. This subgrid in the lens plane is transported in the source plane using the perturbative lens equation at order 1 (equation 5). The size of the grid in the source plane is adapted to the resolution of the grid in the lens plane. The grid size in the source plane has to be small enough to preserve the smallest details of the original grid in the image plane. Basically a resolution element in the image plane (a pixel grid) is transformed to a complex figure in the source plane. This complex figure has a minimum dimension, and this dimension should be at least larger than the source plane grid size. Considering now all the grid pixels in the image plane, we compute the minimum of the local pixel dimension. This minimum gives some idea about the size of the grid in the source plane. In practice to ensure a proper conservation of information, the actual grid size has to be smaller and thus should be divided using a proper scaling factor. This scaling factor should be large enough but not too large, to avoid oversampling the information. To determine this scaling factor, numerical experiments were performed using various scaling factors, 1.5, 2 and 3. Each time and for each scaling factor the process of computing the solution was repeated by oversampling by a factor of 2 (or equivalently multiplying the scaling factor by 2). The criterion used to assess the relevance of a given scaling factor is to compare the regular solution and the oversampled solution, which should deviate only by the typical amplitude of the noise fluctuations. The result of the numerical experiments indicates that a factor of 2 is the minimum in order to obtain a consistency between the solution and the over-resolved solution. This numerical process is rather costly but has the merit of being robust. In some areas, the grid size has to be adapted by extending the bin size in order to have at least a few points from the image plane falling into the bin in the source plane. When several values fall in the same cell of the source plane (which is by definition the case when several images are formed), the different values are averaged. Note that averaging the values coming from the image plane is actually equivalent to an estimation of the source grid point weight by least-squares minimization. In effect the source model can be described as a sum of local grid bin, these images do not overlap and thus have no cross terms in the least-squares matrix. As a consequence, the least-squares weight is directly the cross product of the data with the image of the source local bin, which itself is equivalent to the sum of pixel values covering the image. As a consequence, this averaging process is actually equivalent to a semilinear process as described in Warren & Dye (2003), with the basis functions for the source being the bin in the source plane. Once a source model is constructed, the corresponding image is formed by estimating the values of the pixels on the finer grid in the lens plane. The finer grid image is integrated to produce an image at the initial resolution.

2.3 Image deconvolution

The source and image reconstruction procedure we described ignores the problem of the convolution of the image with the point spread function (PSF). A numerical model of the PSF is reconstructed using the TINY TIM software (Krist, Hook & Stoehr 2011) and another one is obtained by using the empirical model of Anderson (2016). In this work, we use these two different models in order to check for the influence of the PSF model on the result. Note that the Anderson (2016) empirical model is not available for the *F*475*W* filter but only for the *F*675*W* and *F*875*W* filters. It is important to note that the difference between the two PSF models is small. The Anderson (2016) PSF model is a little sharper than the TINY TIM PSF model, with a typical difference in relative width of about a few per cent. To correct for the effect of the PSF convolution on the image, an iterative Van Cittert method (Van Cittert 1931) is implemented. The Van Cittert correction is the difference between the *HST* image and the image of the source. In order to correct the source model, this correction is sent back to the source plane. An image of the corrected source is computed and the method is iterated again. The number of iterations in the deconvolution process should be optimized to reach the optimal signal-to-noise ratio. The signal is evaluated by measuring the amplitude of the density peaks in the source reconstruction. The deconvolution process narrows the peaks and thus increases the central value, thus the higher the peak the more the deconvolution process has operated. On the other hand, the noise is evaluated in low-signal areas of the source and also using the control points. After a certain number of iterations no signal improvement is obtained but only the noise amplitude is increased. It is found that below 5 iterations some signal is lost, while above 10 iterations only noise is increased. As a consequence, the optimal number of iterations is between 5 and 10. Note that in this process the noise is entirely the noise present in the data, and at each step the noise sent back to the source plane is the actual level of the Paley decomposition of this noise. The Paley decomposition refers to a simple wavelet transform also known as the Littlewood–Paley wavelet, see Daubechies (1992) for more details. The Paley decomposition of the noise does not change and thus it
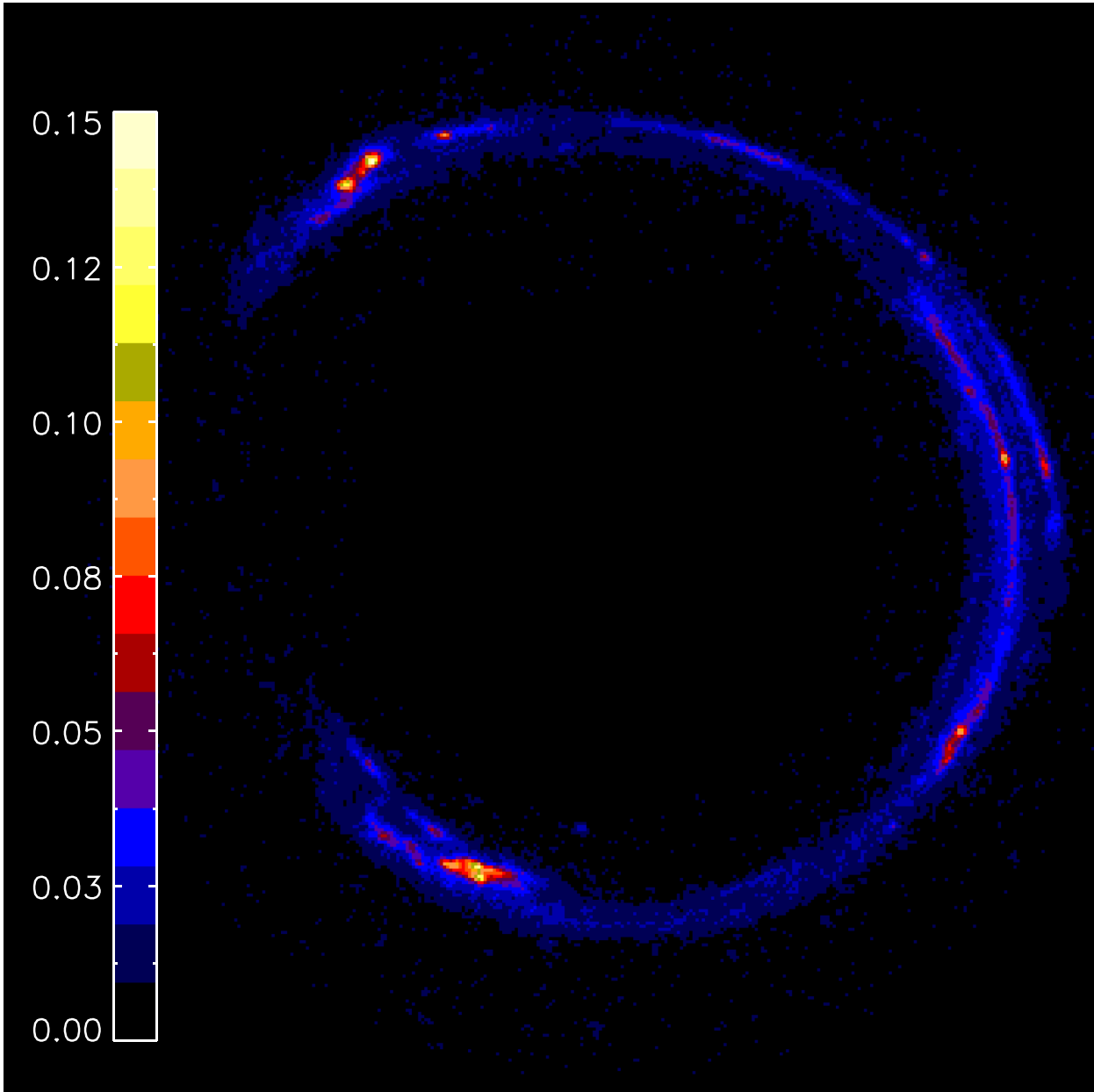
Figure 1. The *HST* WFC3 image of the cosmic horseshoe lens taken using the *F*475*W* filter.

is not useful to re-estimate each time the optimal number of itera-tions. An important point is that it would be quite risky not to fix the number of iterations. The obvious risk is that the method would not converge or converge to a false solution since a jump in the number of iterations would result in random fluctuations with no physical meaning. Finally, a number of eight steps were adopted; however, changing this number and taking any number between 5 and 10 does not produce significant changes.

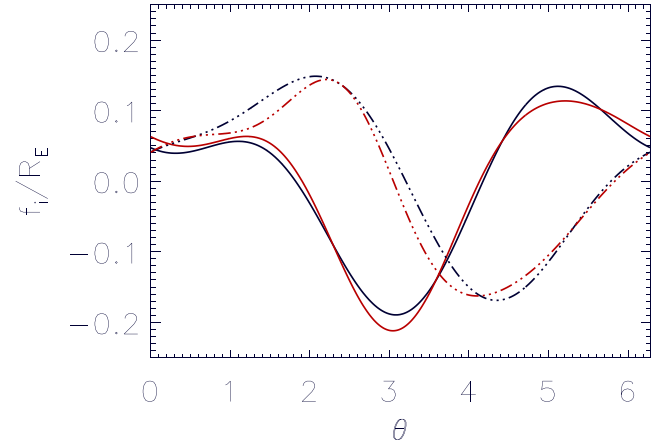### 2.4 Accurate numerical estimation of the fields

The numerical fit of the data is performed on a selected area. First, the area occupied by the arc is identified by applying a threshold and then this area is extended by performing a convolution with the pixels above the threshold. This convolution procedure ensures that the outliers of the arc are properly included. In addition to the

data point in the selected area, a number of points located in a ring around the arc are also included. These points correspond to dark areas and as such are useful to enforce the constraint that no images are formed in dark areas. These points will be designated as control points. Note that initially the solution guess is built to form no im-age in the dark areas. As a consequence, controlling that no images are formed in the dark areas is more a matter of precaution and also a precaution to avoid the development of false solutions. It is also useful to estimate the statistic of the noise for the control points. The reconstruction of the solution is a complex numerical process, it is thus interesting that this process itself does not generate spu-rious noise. Since the control points are located in dark areas, the statistics of the noise should remain that of pure noise, any devia-tion indicating a problem. This control of the noise statistics is an additional precaution to ensure that no spurious solution is gen-erated. In the first step of the numerical refinement the fields are
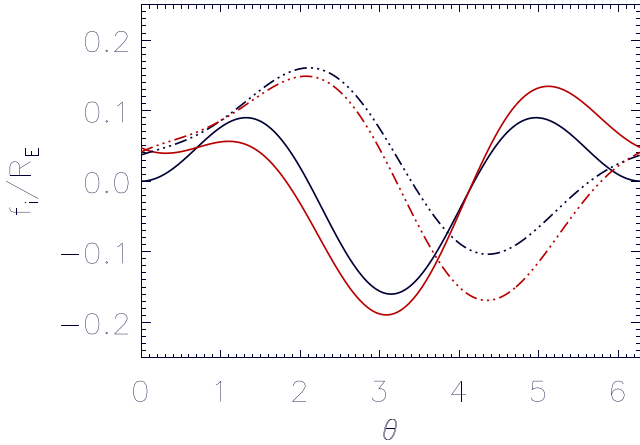
Figure 2. The initial guess (dark colour) superimposed with the refined solution at Fourier order 2. The field $\frac{df_0}{d\theta}$ is represented by a continuous line, while f_1 is represented with a dotted line.

Figure 3. The solution for the fields at order 2 (dark colour) superimposed with the refined solution at Fourier order 4. The field $\frac{df_0}{d\theta}$ is represented by a continuous line, while f_1 is represented with a dotted line.

modelled by order 2 Fourier series. Given a model of the fields a reconstruction of the source and images of the source are performed using the method described is Sections 2.2 and 2.3. Using the difference between the reconstructed images and the *HST* images a weighted chi-square is estimated. The weights applied in the chi-square estimation are computed using the noise expectation (see Section 2.5). The reconstruction is applied first to the blue (*F475W*) *HST* WFC3 calibrated image (see Fig. 1). The main asset of the blue band is that the residual contribution of the central deflector to the flux of the arc is very faint. At this point, it is important to note that the reconstruction process that we will now describe for the *F475W* band is applicable to the *F675W* and *F875W* bands. As a consequence, the results for these two former bands will be given directly without needing a redescription of the process each time. Despite the weakness of the outer wings from the main galaxy, a Sérsic model was fitted to the deflector and the contribution around the arc was subtracted (see Figs 12–14). The typical amplitude of the subtraction is at the noise level. The refinement process is performed on this processed image of the arc by using the Simplex method (Nelder & Mead 1965). The approximate guess for the coefficients is used to initialize the Simplex, and start the minimization process of the chi-square. It is important to note that the result of this minimization process does not produce significantly different results if the initial guess is changed. Experiments were conducted by changing the parameters of the initial guess by an amplitude that is of the order of the refinement. The results of these experiments indicate a general convergence to the same solution. The stability of the solution is due to the perturbative approach. This method provides a fundamental reduction of the degeneracy problem encountered in the modelling of gravitational lenses. The result of the Simplex minimization is presented in Figs 2 and 3. In the next step, the expansion in Fourier series of the numerical solution is extended to higher order. Fir st it is extended to order 3, the initial guess is the second-order solution with zeros for the third-order terms. Similarly the solution is extended to order 4. In the fit of the Fourier expansion of the fields, an important problem is to evaluate the reasonable number of parameters to adjust with respect to the information and constraints available. The constraints available in this lens come from the conjugate images of the source local density peaks. In Fig. 10, we observe four main density peaks inside the caustics and seven outside. Since there are three con-

Table 1. The χ^2/dof as a function of the order of the Fourier series expansion of the fields for the three different filters.

Order	2	3	4
χ^2/dof (*F475W*)	2.29	1.38	1.28
χ^2/dof (*F675W*)	1.88	1.32	1.22
χ^2/dof (*F875W*)	2.14	1.52	1.47

straints per image (the coordinates and the amplitude) and that if *N* image are formed (*N*−1) effective equations exists, we find a total of 45 constraints. This total number of constraints largely exceeds the number of parameters of the order of 4 Fourier expansion that contains 17 parameters. We will now turn to the essential discussion of the noise and statistical properties of the solutions.

## 2.5 Noise and statistical properties of the solutions

The statistical expectation of the noise in the image σ_0 corresponds to the photon noise derived from the photon counts. Using this statistical expectation for the noise the chi-square and χ^2/dof are estimated for the different models (see Table 1). The corresponding histogram of the normalized deviations for each model is presented in Fig. 4. For comparison, the χ^2/dof for the two other filters available in the *HST* archive are also presented in Table 1. There is a very marked difference between the χ^2/dof obtained at orders 2 and 3. The gain in χ^2 obtained by going to order 4 is much less spectacular. This suggests that the order 3 terms are important and significant. To test this hypothesis, it is essential to estimate the amplitude of the noise fluctuation for the Fourier coefficients. The least-squares minimization is non-linear, but can always be linearized near the optimal solution. Let us define the optimal solution:

$$\boldsymbol{P} = [\alpha_{0,i}, \beta_{0,i}, \alpha_{1,i}, \beta_{1,i}]_{\{i=1..4\}}.$$

We linearize the lens model $M(\boldsymbol{P})$ near $\boldsymbol{P}$:

$$M(\boldsymbol{P} + \mathrm{d}P) = M(\boldsymbol{P}) + \sum_n \frac{\partial M}{\partial p_n} \mathrm{d}p_n, \qquad (10)$$

where p_n and dp_n are the components of the vectors P and dP, respectively. The model in equation (10) is formally equivalent to a linear least squares with basis vectors, $\frac{\partial M}{\partial p_n}$. As a consequence, the
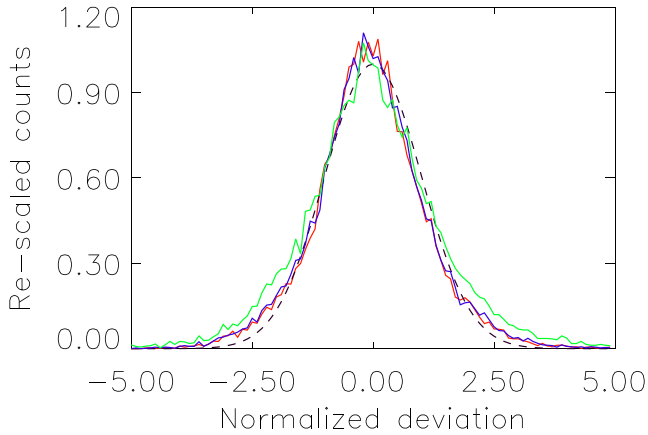
Figure 4. Histograms of the normalized deviations for the order 2 (green), order 3 (blue) and order 4 (red). The dashed line corresponds to the theoretical Gaussian expectation.
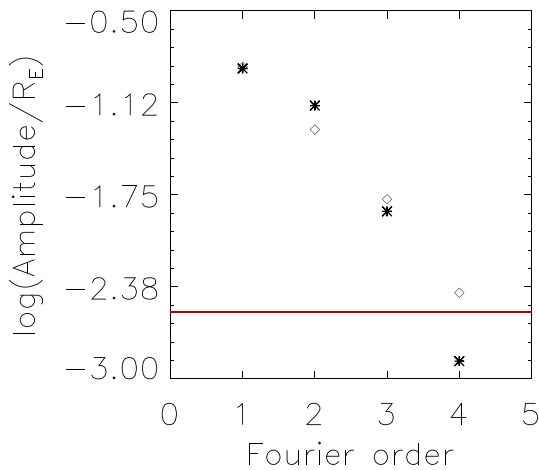
Figure 5. The amplitude of the Fourier components as a function of the order of the component. The red line represents the 4σ limit. The asterisks represent the components of $\frac{df_0}{d\theta}$, while the diamonds represent the components of f_1.

errors on the parameters are directly the diagonal elements of the inverse of the corresponding normal least-squares matrix. Explicitly, the normal least-squares matrix elements are

$$A_{ij} = \sum_{\text{Image}} \frac{1}{\sigma_0^2} \frac{\partial M}{\partial p_i} \frac{\partial M}{\partial p_j}.$$

Defining $C = A^{-1}$ the variance associated with parameter p_n is, $\sigma_n = C_{nn}$. A numerical estimation of the matrix elements A_{ij} shows that the associated variance elements σ_n are almost constant and equal to $0.5 \, 10^{-3}$ in units of the Einstein radius R_E. The calculation of the variance of the Fourier components allows a direct estimation of the significance of the components at different orders (see Fig. 5). It is clear in Fig. 5 that components of order $n \geq 3$ are well above the 4σ limit. This is a direct confirmation that the order 3 components are very significant and essential to the modelling of this lens. The amplitude of the order 4 component is not significant for the $\frac{df_0}{d\theta}$ field and is only marginally significant for the f_1 field.

3 ANALYZING THE SOLUTION

The structure of the fourth-order solution is now explored in details. The reconstruction for the *F475W* filter in the lens plane is presented in Fig. 6. A comparison of the fine details of the solution and the original *HST* image in the *F475W* band is presented in Fig. 7. A general appreciation of the quality of the reconstruction is also provided by the difference image with the original image (see Fig. 8). For consistency, the solution in the *F475W* band is compared to the solutions in the 2 other bands, see Fig. 15 and Table 2 for more details. The comparison shows that the solutions in the different bands are compatible considering the noise fluctuations. Similarly, the consistency between the solutions in the same band for the two different PSF models is evaluated in Fig. 15 and Table 2. The results obtained indicate that the solutions in the same band for different PSF are consistent within the expectation of the noise fluctuations. It is interesting to note that the result is not influenced by changing slightly the PSF model and that the method is stable with respect to small changes in the PSF model. The reconstruction in the source plane is presented in Fig. 9. Note that the source reconstruction was obtained by co-adding the reconstructions obtained in the three bands. For a more detailed view of the source, see Fig. 10. It is interesting to note that Bellagamba, Tessore & Metcalf (2017) derived a quite similar source model using a completely different approach.

3.1 Effect of degeneracy induced by higher order perturbative terms

The first-order perturbative expansion neglect the effect of higher order terms in the expansion. For most gravitational arcs, it is possible to reduce the higher order expansion to a first-order expansion. Which means that some small degeneracy problem is present. The amplitude of the correction due to higher order terms is evaluated using realistic (NFW) models for the halo of the deflector. Let us consider a purely elliptical NFW halo that by definition has no third-order distortion of its isophotes. We consider the perturbative expansion of this elliptical NFW model to perturbative order 2. The forced reduction of this expansion to order 1 introduces additional degenerate terms in the expansion. Could these terms be responsible for the order 3 terms that we observe in the lens model? The expansion at order 2 reads (Alard 2016)

$$r_S = \left(\kappa_2 \, dr - \kappa_3 \frac{dr^2}{2} - \tilde{f}_1 - f_2 dr \right) \boldsymbol{u}_r$$

$$- \left(\frac{d\tilde{f}_0}{d\theta} + \left(\frac{df_1}{d\theta} - \frac{df_0}{d\theta} \right) dr \right) \boldsymbol{u}_\theta$$
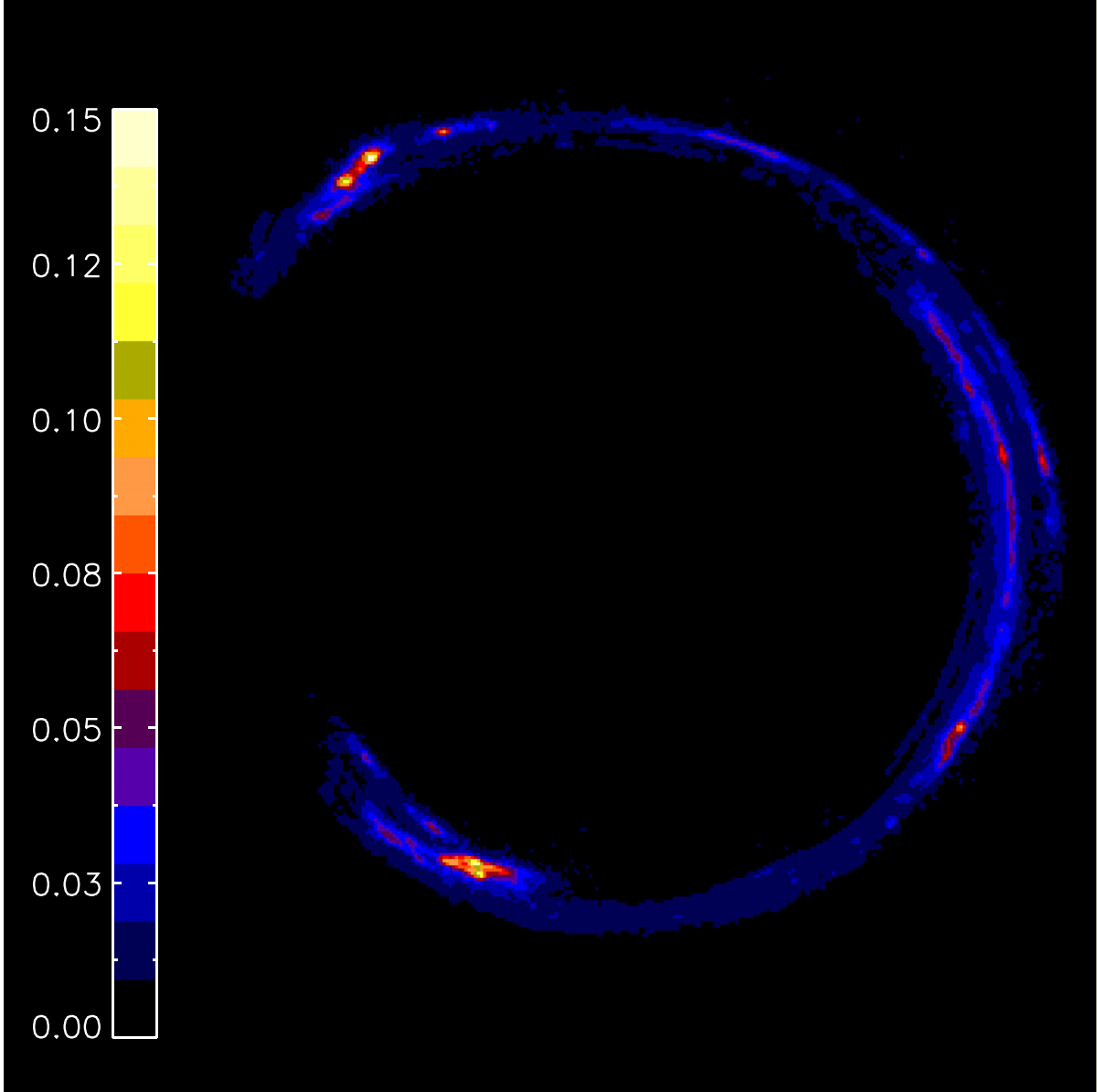
$$\kappa_3 = \left[\frac{d^3 \psi_0}{dr^3} \right]_{r=1} \tag{11}$$

and

$$f_2 = \frac{\partial^2 \psi}{\partial r^2}.$$

Assuming a thin arc model,

$$dr = \frac{\tilde{f}_1}{\kappa_2} + \epsilon dr_2. \tag{12}$$

The arc in this lens presents a thickness in the radial direction that is small with respect to the general displacement of the fields. Thus, equation (12) is certainly appropriate for an evaluation of the amplitude of the third-order terms. Introducing equation (12) in

Figure 6. The reconstructed image in the *F475W* band.

equation (11) leads to (Alard 2016)

$$
\tilde{r}_S = \left(\kappa_2 \mathrm{d}r_2 - \kappa_3 \frac{\tilde{f}_1^2}{2\kappa_2^2} - \frac{\tilde{f}_1 f_2}{\kappa_2} \right) \boldsymbol{u}_r \\
- \left(\frac{\mathrm{d}\tilde{f}_0}{\mathrm{d}\theta} + \left(\frac{\mathrm{d}f_1}{\mathrm{d}\theta} - \frac{\mathrm{d}f_0}{\mathrm{d}\theta} \right) \frac{\tilde{f}_1}{\kappa_2} \right) \boldsymbol{u}_\theta. \tag{13}
$$

Equation (13) is equivalent to equation (7) provided that the following substitutions are performed:

$$
\begin{cases}
\tilde{f}_1 \rightarrow \tilde{f}_1 + \kappa_3 \frac{\tilde{f}_1^2}{2\kappa_2^2} + \frac{\tilde{f}_1 f_2}{\kappa_2} \\
\frac{\mathrm{d}\tilde{f}_0}{\mathrm{d}\theta} \rightarrow \frac{\mathrm{d}\tilde{f}_0}{\mathrm{d}\theta} + \left(\frac{\mathrm{d}f_1}{\mathrm{d}\theta} - \frac{\mathrm{d}f_0}{\mathrm{d}\theta} \right) \frac{\tilde{f}_1}{\kappa_2}
\end{cases} . \tag{14}
$$

To evaluate the amplitude of the additional terms in equation (14), we use the NFW halo model. The potential for an NFW halo reads (Meneghetti, Bartelmann & Moscardini 2003)

$$
\begin{cases}
\phi(u) = \frac{1}{1 - \ln(2)} g(u) \\
u = \sqrt{\left((1 - \eta)x^2 + (1 + \eta)y^2 \right)}
\end{cases} . \tag{15}
$$

The parameter η is related to the ellipticity of the halo. The potential normalization implies that the associated Einstein radius is equal to the typical halo size, which is a common situation for gravitational lenses. The definition of the function $g(u)$ reads

$$
g(u) = \frac{1}{2} \ln \left(\frac{u}{2} \right)^2 + \begin{cases}
2\arctan^2 \left(\sqrt{\frac{u-1}{u+1}} \right) & u \geq 1 \\
-2\operatorname{arctanh}^2 \left(\sqrt{\frac{1-u}{u+1}} \right) & u < 1.
\end{cases} \tag{16}
$$
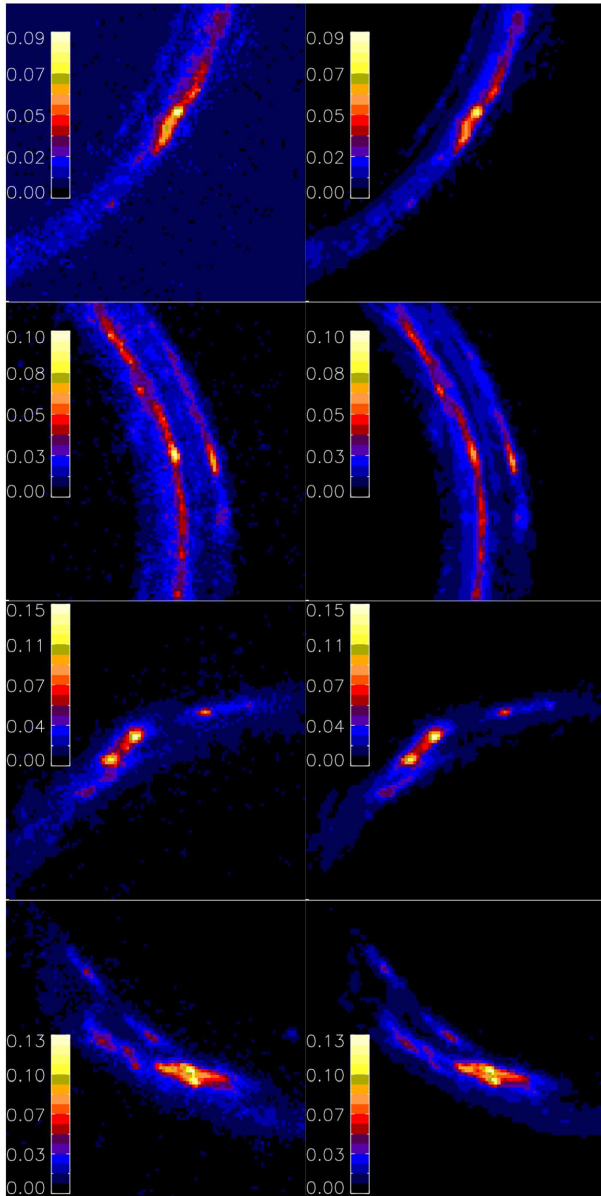
Figure 7. Details of the *HST* image in the *F*475*W* band (left) compared with the corresponding area in the reconstructed image (right).

Using the NFW potential (see Meneghetti et al. 2003) defined in equation (15) the functional, f_0, f_1 and f_2 are calculated. The result is introduced in equation (14) to evaluate the correction due to the order 2 terms. For the f_1 field the correction is $\simeq 0.2x_0\eta$ and $\simeq 0.2y_0\eta$ for the $\cos(3\theta)$ and $\sin(3\theta)$ terms, respectively. Where (x_0, y_0) are the source impact parameters. The correction for f_0 is of smaller amplitude. For this lens, $x_0 \simeq 0.03$, $y_0 \simeq 0.13$ and $\eta \simeq 0.07$. As a consequence, the largest third-order term is only of $\simeq 2 \times 10^{-3}$ that is similar to the 4σ noise limit. Thus, it is clear from this analysis that the observed third-order terms in this lens are not the consequence of neglecting higher order terms in the perturbative expansion.

4 INTERPRETATION OF THE LENS MODEL

The reconstruction of the lens is directly related to the geometry of the potential. The potential iso-contours equation, $dr = -f_0$

(Alard 2009) is represented in Fig. 11. By relating the perturbative expansion to the multipole expansion (Alard 2009), it is simple to reconstruct the potential generated by the distribution of matter inside the Einstein circle (inner) and outside the Einstein circle (outer). The iso-contours for the outer potential are represented in Fig. 11, they are close to the potential iso-contours. As a consequence, most of the potential is generated outside the Einstein circle, this is even more true for the third order terms where over 90 per cent of the potential originates in the outer distribution. The outer distribution includes a number of galaxies belonging to a small group of galaxies where the central deflector is the main element (Belokurov et al. 2007; Spiniello et al. 2011; Agnello, Auger & Evans 2013,). Thus, it is interesting to evaluate the perturbations due to the accompanying galaxies in the group. The first step is to identify the galaxies around the lens. A general search for galaxies in a radius corresponding to the size of the group ($\simeq 1$ arcmin; Belokurov et al. 2007) was performed. Objects were identified by looking for local maxima's in a moving mesh with a size of 25 pixels. Punctual objects with corresponding width not significantly larger than the PSF were eliminated. The Petrosian magnitude (Petrosian 1976) is evaluated for the remaining objects in the different photometric bands. The contribution of each galaxy to the lensing fields is estimated by assuming a proportionality relation between the red (*F*875*W*) flux and the total mass. The potential of the perturbator is evaluated by considering the three following models: (i) a spherical isothermal sphere, (ii) a point mass and (iii) a spherical NFW profile. For each model, the lensing fields f_1 and $\frac{df_0}{d\theta}$ are evaluated using equation (9). It is interesting to note that about 90 per cent of the contribution to the lensing perturbation is due to elliptical galaxies with colour similar to the central galaxy. Considering that the mass-to-light ratio of elliptical galaxies dependence is weak as a function of the galaxy size (see Djorgovski & Davis 1987; Dressler et al. 1987; Bender, Burstein & Faber 1992; Cappelari et al. 2013; Desmond & Wechsler 2017), a good approximation is to assume a constant mass-to-light ratio for this subgrid of galaxies. The flux normalization factor is applied by dividing each flux by the flux of the main galaxy. As a result, all masses are expressed in units of the main galaxy mass. In this reconstruction another source of error comes from the ellipticity of the potential. For an axis ratio of the ellipse equal to $1 + \eta$, the typical percentage in error induced by the ellipticity on the fields f_1 and $\frac{df_0}{d\theta}$ is of the order of η. For dark matter haloes a typical value is $\eta \simeq 0.2$. The uncertainty on mass is at least of about 10 per cent since the flux-to-mass proportionality relation applies only approximately to elliptical galaxies. As a consequence, an error of about 25 per cent at least is expected for this kind of model. An estimation of the fields for the different models is presented in Table 3. The point mass and NFW model predictions for the third-order coefficients are in general agreement with the values reconstructed from the lens model. As shown by the relative errors presented in Table 4, the isothermal model exceeds the error expectation, while the errors for two other models are consistent with the 20 to 30 per cent relative error expectations. It is interesting to compare these results with Dye et al. (2008), who could not find any contribution coming from the other group members. However, Dye et al. (2008) used low-resolution images taken from the ground and could not reach the level of accuracy obtained with the *HST* images. A more recent analysis of the cosmic horseshoe lens was performed by Brewer, Huijser & Lewis (2016), who could not find substantial evidence for substructures in the lens. However, the problem of evaluating the contribution of substructures in the lens is not equivalent to the evaluation of the group members contributions. The elements of the group are more massive than substructures and
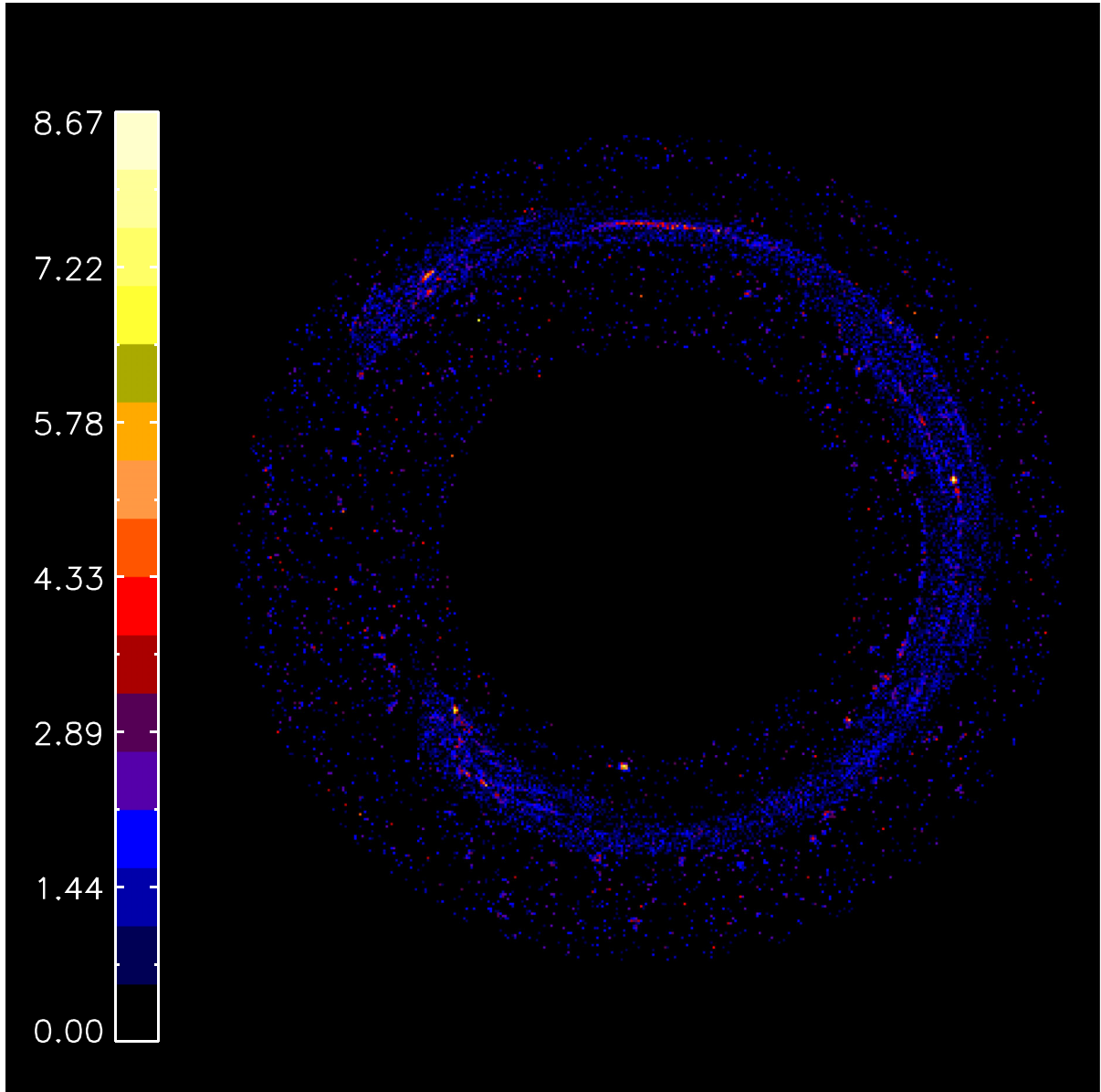
Figure 8. The absolute value of the difference between the *HST* image and the reconstructed image normalized by the noise expectation (*F475W* band). Note that additional points were added in pure noise area as control points (one-third of total points).

Table 2. The reduced chi-square of the difference between the Fourier coefficients for different photometric bands (first two columns), and for the 2 PSF models (last two columns).

| Bands	*F875W*– *F475W*	*F675W*– *F475W*	*F875W*–PSF(1)– *F875W*–PSF(2)	*F675W*–PSF(2)– *F675W*–PSF(2)
σ	1.46	0.93	0.75	1.2

on average are situated at larger distances than substructures. Thus, it is not surprising that the Brewer et al. (2016) analysis failed to identify the contribution of the group members.

5 CONCLUSION

The perturbative method allowed the reconstruction of the cosmic horseshoe lens without making any particular assumptions about the
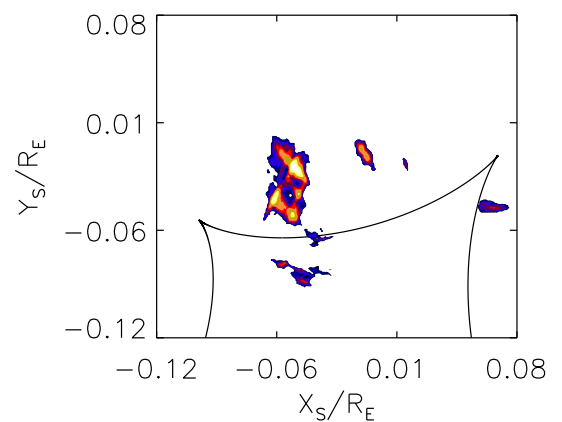

Figure 9. The reconstruction of the source superimposed with the caustic system of the lens.
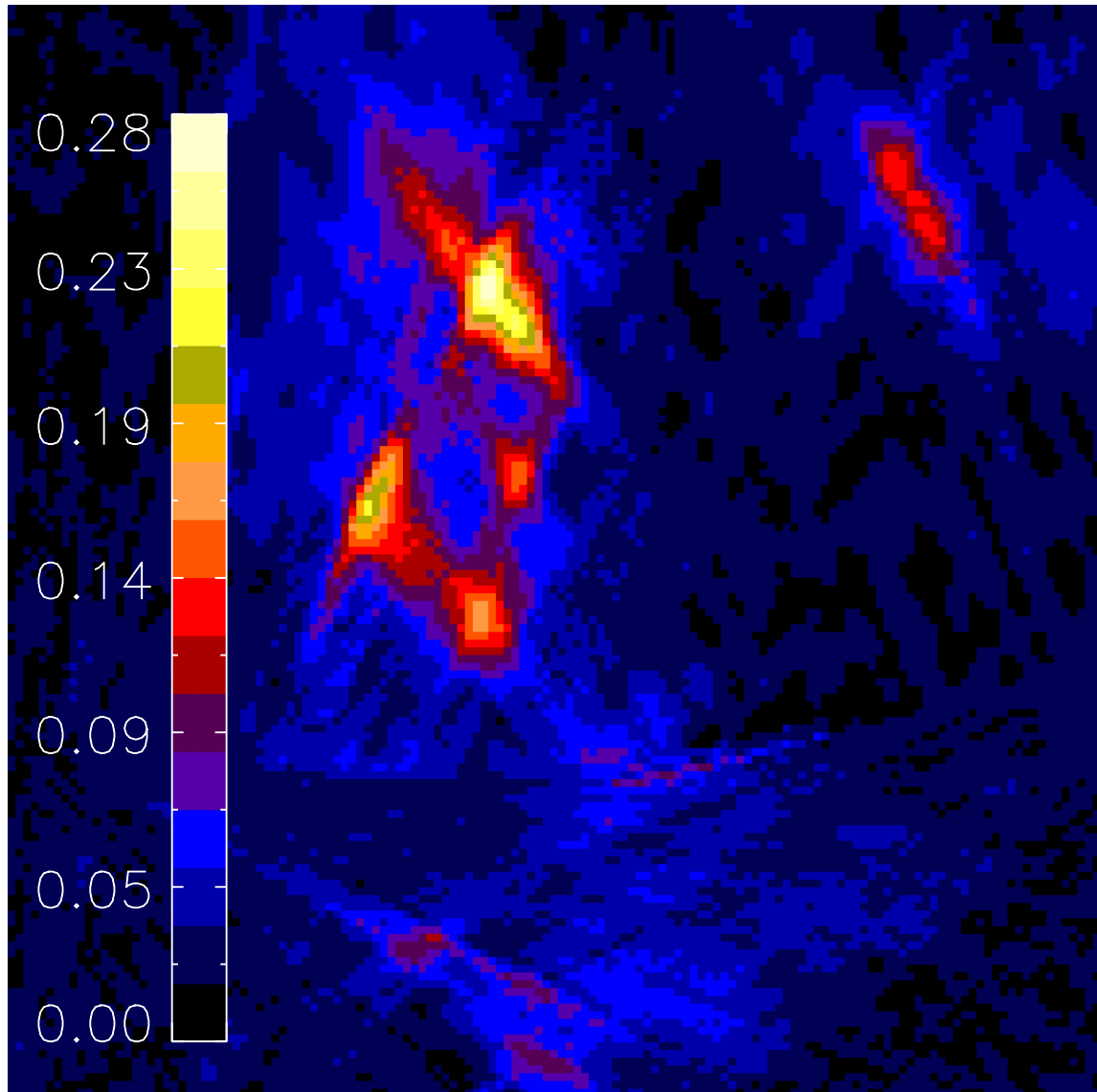
Figure 10. A detailed view of the source main component.

nature of the lens. The inclusion of third-order terms was dictated only by the necessity to optimize the chi-square. These third-order terms were related to the group contribution later in the analysis, but it was not necessary to make any hypothesis about the group contribution when reconstructing the lens. In this case, the group is made of quite a large number of galaxies and trying to make an extensive model including each object would require too many parameters. Such models including many parameters are generally plagued with degeneracy issues, which is a constant re-occurring problem in conventional gravitational lens analysis. This analysis does not have to include all these parameters but reduces the lens to a number of fundamental parameters. It is clear that this minimal set of parameters (basically the expansion of the fields to order 3) corresponds to the expectation of many models, when the model includes more parameters than the fundamental parameters (which would be the case here when modelling all the group). As a consequence, it is clear that the perturbative approach is a method of choice for complex systems. The perturbative approach allows a general, non-degenerate, fast and simple analysis of any gravitational lens system. It is important to note that even in the case of
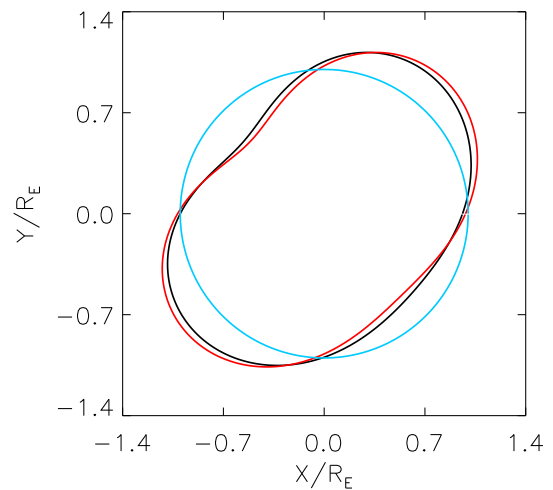

Figure 11. The potential iso-contours (red line) superimposed with the iso-contours corresponding to the outer distribution (black line). A circle with radius unity is plotted for reference (blue line).

Table 3. Models of the perturbation due to the group members.

Model	$\frac{\mathrm{d}f_0}{\mathrm{d}\theta};\cos(3\theta)$	$\frac{\mathrm{d}f_0}{\mathrm{d}\theta};\sin(3\theta)$	$f_1;\cos(3\theta)$	$f_1;\sin(3\theta)$
Isothermal	0.002	− 0.0073	0.0071	0.001 75
Point mass	0.01	− 0.0123	0.0126	0.01
NFW	0.0094	− 0.011	0.011	0.0096
Reconstruction	0.011	− 0.0078	0.0089	0.014

Table 4. Relative deviation from reconstructed coefficients for different model of the perturbators potential.

Model	$\frac{\mathrm{d}f_0}{\mathrm{d}\theta}$	f_1
Isothermal	0.68	0.75
Point mass	0.36	0.32
NFW	0.26	0.3
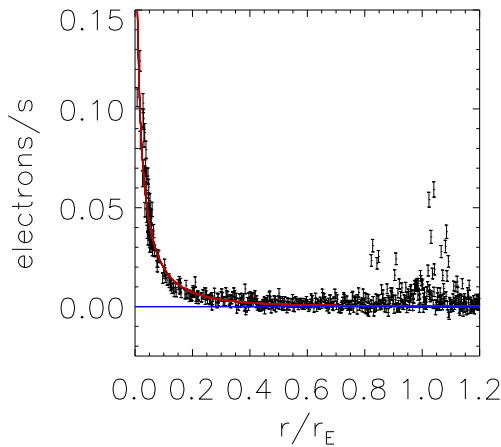
Figure 12. The fit of a Sérsic profile for the *F475W* band. The corresponding index of the Sérsic profile is 0.38. The base line represents the zero level in flux. Note the scatter in the data points due to the presence of the arc near the position $\frac{r}{r_E} \simeq 1$.
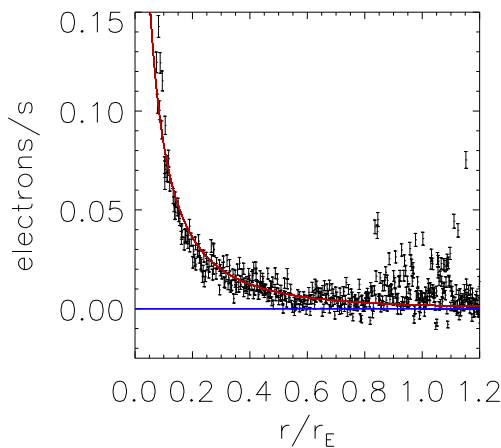
Figure 13. The fit of a Sérsic profile for the *F675W* band. The corresponding index of the Sérsic profile is 0.36. The base line represents the zero level in flux. Note the scatter in the data points due to the presence of the arc near the position $\frac{r}{r_E} \simeq 1$.
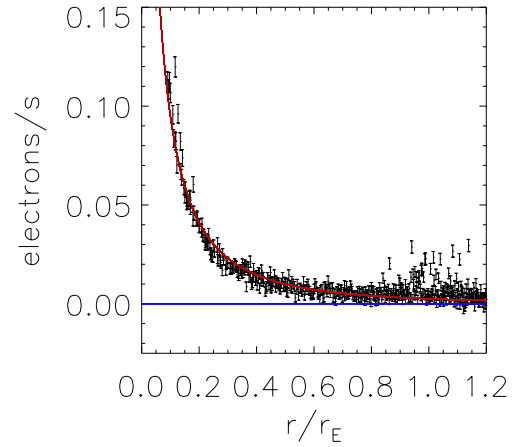
Figure 14. The fit of a Sérsic profile for the *F875W* band. The corresponding index of the Sérsic profile is 0.31. The base line represents the zero level in flux. Note the scatter in the data points due to the presence of the arc near the position $\frac{r}{r_E} \simeq 1$.
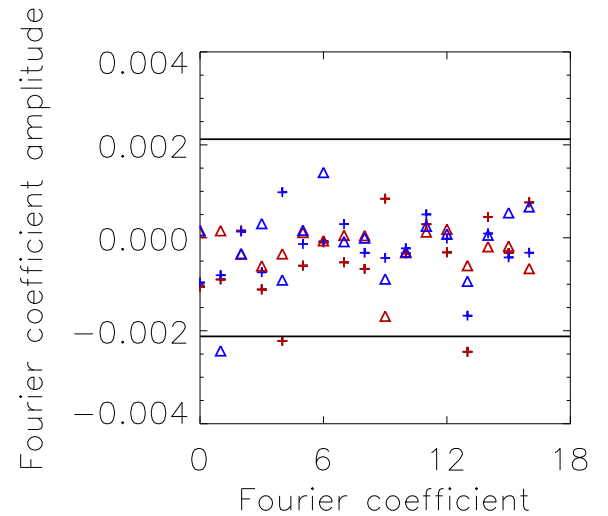
Figure 15. The difference between the Fourier coefficients obtained in the *F475W* band and the *F875W* band (red cross), overplotted with the difference between the *F475W* and *F875W* band (blue cross). The difference between the Fourier coefficients for two different PSF models is also represented, for the *F875W* band (red triangles), and for the *F675W* band (blue triangles). The two horizontal lines represent the 3σ limit.

an a priori simple lens system it is useful to apply the perturbative method since this method could reveal unexpected complex contributions. Essentially in the same way that the contribution of the group was discovered without making any initial hypothesis about the presence of the group.

ACKNOWLEDGEMENTS

REFERENCES

Agnello A., Auger M. W., Evans N. W., 2013, MNRAS, 429, L35

Alard C., 2007, MNRAS, 382, L58

Alard C., 2009, A&A, 506, 609

Alard C., 2010, A&A, 513, 39

Alard C., 2016, preprint (arXiv:1607.01365)

Anderson J., 2016, 'Empirical Models for the WFC3/IR PSF', Instrument Science Report WFC3 2016-12. Available at: http://www.stsci.edu/hst/wfc3/documents/ISRs

Barnabè M., Czoske O., Koopmans L., Treu T., Bolton A., Gavazzi R., 2009, MNRAS, 399, 21

Barnabè M., Czoske O., Koopmans L., Treu T., Bolton A., 2011, MNRAS, 415, 2215

Bellagamba F. Tessore N., Metcalf R., 2017, MNRAS, 464, 4823

Belokurov V. et al., 2007, ApJ, 671, L9

Bender R., Burstein D., Faber S. M., 1992, ApJ, 399, 462

Birrer S., Lilly S., Amara A., Paranjape A., Refregier A., 2014, ApJ, 793, 12

Birrer S., Amara A., Refregier A., 2015, ApJ, 813, 102

Bolton A. et al., 2012, ApJ, 757, 82

Brewer B., Huijser D., Lewis G., 2016, MNRAS, 455, 1819

Brownstein J. et al., 2012, ApJ, 744, 41

Cappellari M. et al., 2013, MNRAS, 432, 1709

Chiba T., Takahashi R., 2002, Prog. Theor. Phys., 107, 625

Czoske O., Barnabè M., Koopmans L., Treu T., Bolton A., 2008, MNRAS, 384, 987

Czoske O., Barnabè M., Koopmans L., Treu T., Bolton A., 2012, MNRAS, 419, 656

Daubechies I., 1992, Ten Lectures on Wavelets. American Mathematical Society, Providence, RI

Desmond H., Wechsler R., 2017, MNRAS, 465, 820

Djorgovski S., Davis M., 1987, ApJ, 313, 59

Dressler A., Lynden-Bell D., Burstein D., Davies R., Faber S., Terlevich R., Wegner G., 1987, ApJ, 313, 42

Dye S., Evans N., Belokurov V., Warren S., Hewett P., 2008, MNRAS, 388, 384

Evans N., Witt H., 2003, MNRAS, 345, 1351

Jackson N., Tagore A. S., Roberts C., Sluse D., Stacey H., Vives-Arias H., Wucknitz O., Volino F., 2015, MNRAS, 454, 287

Krist J., Hook R., Stoehr F., 2011, in Kahan M. A., ed., Proc. SPIE Conf. Ser. Vol. 8127, Optical Modeling and Performance Predictions V. SPIE, Bellingham, p. 81270J

Meneghetti M., Bartelmann M., Moscardini L., 2003, MNRAS, 340, 105

Nelder J., Mead R., 1965, Comput. J., 7, 308

Petrosian V., 1976, ApJ, 209, L1

Saha P., Williams L., 2006, ApJ, 653, 936

Spiniello C., Koopmans L., Trager S., Czoske O., Treu T., 2011, MNRAS, 417, 3000

Suyu S., Marshall P., Hobson M., Blandford R., 2006, MNRAS, 371, 983

Suyu S., Marshall P., Blandford R., Fassnacht C., Koopmans L., McKean J., Treu T., 2009, ApJ, 691, 277

Tagore A., Jackson N., 2016, MNRAS, 457, 3066

Trotter C., Winn J., Hewitt J., 2000, ApJ, 535, 671

Van Cittert P., 1931, Z. Phys., 69, 298

Vegetti S., Koopmans L., 2009, MNRAS, 392, 945

Warren, S., Dye, S.2003, ApJ, 590, 673

Wucknitz O., 2002, MNRAS, 332, 951

This paper has been typeset from a TeX/LaTeX file prepared by the author.